This article has been accepted for publication in a future issue of this journal, but has not been fully edited. Content may change prior to final publication. Citation information: DOI 10.1109/TIM.2021.3136261, IEEE Transactions on Instrumentation and Measurement

Experimental Evaluation of the Forkbeard Ultrasonic Indoor Positioning System

Vincent Thio, *Member, IEEE*, Joaquín Aparicio, *Member, IEEE*, Kjetil Bergh Ånonsen, and Jan Kenneth Bekkeng

***Abstract*—Indoor positioning systems are crucial to provide location based services in areas that are not covered by a Global Navigation Satellite System. Among the many technologies applied to this field, ultrasound has emerged as a potential low-cost, high-accuracy approach to positioning based on trilateration. Several ultrasonic systems have been proposed over the years. Of these, academic systems are typically prototypes that are unavailable to the public, whereas commercial systems generally do not provide characterization test results. In this work, we have conducted a detailed characterization study of a commercial indoor positioning system for smart devices developed by Forkbeard Technologies AS. We tested the system under static and dynamic conditions in a motion capture lab of approximately 150 m^2. We considered different room occupancies, beacon configurations, and device positions. The results, given in terms of 2D absolute errors at different confidence levels, show great variation depending on the aforementioned conditions. The worst case scenario corresponds to a pedestrian in motion in an office setup with 4 beacons, with the phone placed in the pocket. In this case, 80% of the errors were below 143 cm. The best results were obtained under static conditions using 10 beacons, for which 80% of the errors were below 44 cm.**

***Index Terms*—indoor positioning; performance evaluation; ultrasound ranging**

I. Introduction

With the advent of increasingly powerful smartphones and wearable technology, the fields of Real-Time Location Systems (RTLS) and Location Based Services (LBS) have grown significantly over the last couple of decades. Before, LBS were generally limited to outdoor and relatively open areas due to their dependence on a Global Navigation Satellite System (GNSS). Recent developments in Micro-Electro-Mechanical Systems (MEMS), however, combined with a growing implementation thereof in Commercial-Off-The-Shelf (COTS) devices, have expanded these fields towards areas beyond GNSS coverage.

Some of the industries that have adopted LBS in recent years are: healthcare, where it saves time locating equipment or people, increasing productivity [1]; retail, for inventory management and evaluating marketing techniques and shopper behavior [2]; search and rescue missions, performed by unmanned vehicles and robots navigating the environment [3]; logistics and transportation, for cargo tracking and fleet management [4]; and, more recently, contact-tracing applications during a pandemic event [5]–[7]. The increasing interest in RTLS and LBS was highlighted in a recent market report, which predicted an annual growth rate of 22.5% for indoor LBS between 2020 and 2025 [8].

While generic solutions exist for outdoor RTLS, as evidenced by the widespread use of GNSS services such as GPS or Galileo, no such consensus has yet been reached for indoor RTLS. Indoor environments present a broad range of potential use cases, each with its own specifications and corresponding trade-off between design parameters like accuracy, cost, energy efficiency, lag time, infrastructure, and privacy considerations. In order to meet these specifications, different technologies have been developed over the years.

A low-cost solution to the indoor positioning problem is to use the Earth magnetic field and/or artificial magnetic sources to provide location information based on fingerprinting [9], [10]. These systems typically do not require a dedicated infrastructure (when based on the Earth magnetic field), making it easy to implement and scale. The provided accuracy, however, is relatively low and sensitive to changes in the environment, such as metal structures [11]. Another infrastructure-free approach is to use pedestrian dead reckoning techniques based on an Inertial Measurement Unit (IMU) [12], [13]. Nowadays, these low-cost sensors are standardly embedded in smart devices like smartphones. While generally accurate over short time intervals, these sensors are subject to error accumulation due to sensor noise and bias. This requires periodical corrections based on external measurements [11]. Computer vision systems [14], [15] can provide accuracies ranging from room-level to mm–cm. They can however be computationally demanding, suffer under challenging lighting conditions, and may be a concern in privacy-oriented applications. Systems based on visual-light communications may remove the privacy concern [16], [17], but not the dependence on proper lighting conditions. Both systems also require an unobstructed line-of-sight between beacons and the smartphone camera. Wi-Fi [18], [19], Zigbee [20], [21] and Bluetooth [22], [23] systems benefit from the ubiquity of access points and standard sensors embedded in smart devices, but their accuracy is typically in the order of a few meters [11], [24]. Ultra-wideband systems can deliver more accurate positions with median errors between tens of cm to 1 m [25]. These systems require a

This work was supported by the Research Council of Norway under project number 269614. Forkbeard Technologies AS provided the hardware and support, but were not involved in the experiments and evaluation process. The authors declare no conflict of interest.

V. Thio is with the Department of Physics, University of Oslo, 0371 Oslo, Norway (e-mail: vmthio@matnat.uio.no).

J. Aparicio is with the Department of Informatics, University of Oslo, 0373 Oslo, Norway (e-mail: joaqapar@ifi.uio.no).

K. B. Ånonsen is with the Norwegian Defence Research Establishment (FFI), 2027 Kjeller, Norway, and Department of Technology Systems, University of Oslo, 0371 Oslo, Norway (e-mail: kjetil-bergh.anonsen@ffi.no).

J. K. Bekkeng is with the Norwegian Defence Research Establishment (FFI), 2027 Kjeller, Norway, and Department of Physics, University of Oslo, 0371 Oslo, Norway (e-mail: j.k.bekkeng@fys.uio.no).

This article has been accepted for publication in a future issue of this journal, but has not been fully edited. Content may change prior to final publication. Citation information: DOI 10.1109/TIM.2021.3136261, IEEE Transactions on Instrumentation and Measurement

dedicated infrastructure of beacons, which can be costly and create scalability issues [11].

A different group of indoor RTLS is based on acoustic waves, which provide some advantages and disadvantages over electromagnetic waves. Firstly, one advantage is that the speed of sound is several orders of magnitude smaller than the speed of light. Therefore, inaccuracies in Time-of-Flight (TOF) estimation translate to smaller range errors than those produced by systems based on radio-frequency (RF) waves. Thanks to this property, ultrasonic systems can provide up to cm-level accuracy. Secondly, acoustic waveforms behave more consistently indoors than their electromagnetic counterparts, since they are heavily attenuated and reflect on virtually all surfaces. This natural property can be a strong advantage when room-level accuracy is the primary goal. A drawback of this property is that it creates complex interference terms at the receiver. Adding to this complexity is the Doppler effect, caused by a moving transmitter and/or receiver [11]. Thirdly, hardware for common working frequencies, between 10–50 kHz, is low-cost and readily available. This eases the scalability issue for large areas [26]. Moreover, if the frequency of the waves is around 18–20 kHz, then a standard smartphone can be used as transmitter/receiver. This reduces the need for specially designed hardware like tags, in contrast to ultra-wideband systems, for example. A potential disadvantage is that the bandwidth of an acoustic wave is very limited, in particular when using the narrowband channels accessible to smartphones. This narrower bandwidth, combined with the low sampling speeds required for near ultrasound reception, can however be favorable from a power consumption perspective. Finally, since audio processing is supported as a background process on smartphones, and audio signals readily propagate through textiles, an acoustic positioning system may also operate in-pocket. Overall, these challenging phenomena make acoustic positioning an active research topic [27], [28].

In this work, we present the results of a characterization study of the commercial indoor positioning system developed by Forkbeard Technologies AS (Oslo, Norway) [29]. We have conducted a range of experiments in a testing area equipped with this positioning system and a Motion Capture (MoCap) system to provide ground truth reference. The system performance was evaluated under static and dynamic conditions, considering the effects of beacon placement and quantity, infrastructure and physical barriers, and position of the phone on the carrier. The main contributions may be summarized as follows: 1) a detailed statistical analysis under static conditions, 2) extensive testing for two realistic dynamic scenarios, and 3) accurate error calculation based on a MoCap system.

The rest of the paper is structured as follows: Section II gathers the related work, and Section III gives an overview of the Forkbeard positioning system and main components of the algorithm. Section IV describes the testing environment and the experimental setup. Results and discussion are given in Section V, with conclusions and future work outlined in Section VI.

II. Related work

Ultrasonic ranging systems date back to the 1970s [30], and were popularized during the 1980s with the introduction of the pulse-echo systems from Polaroid and Yodel Technologies [31], [32]. The first Ultrasonic Indoor Positioning Systems (UIPS) were presented at the end of the 1980s [33], [34]. In general, UIPS can be classified into two main categories: centralized, in which a central unit computes the location of the device [35], and decentralized, in which the calculations are performed on the device itself [28], [34]. Privacy-oriented RTLS generally fall into the second category. Since the 1980s, most of the known UIPS are academic prototypes, many of which provide clearly defined experiments and results, thereby allowing for proper performance assessment. We will focus here on systems for smart devices that use similar center frequencies and testing areas for evaluation.

The system described by [36] used four transmitters and a smartphone as receiver. The synchronized transmitters simultaneously sent a unique ID by chirp modulation. The smartphone, which was not synchronized to the transmitters, was placed on a stand from where it recorded the received signals. The data were then sent to a computer for later processing. A grid of 25 points was considered for two rooms of respectively 25 and 400 m^2. Five measurements were taken per grid point. 95% of the errors were reported below 15 cm in the small room, and below 3 m in the large room. The architecture presented in [37] consisted of a set of synchronized receivers placed at fixed positions in a room. A smartphone was assigned a unique ID upon entering the room, which it transmitted by chirp modulation. The microphones sent this information to a central unit, which computed the smartphone location. Seven receivers were placed in a clear test area of 100 m^2. The smartphone followed a trajectory of 14 m, covering ca. 35 m^2 of the test area, with an average deviation of 34 cm. ARABIS [35] consisted of a set of beacons deployed at fixed, known positions, which transmitted their signals sequentially to avoid collisions. Upon data detection, a smartphone calculated the time-stamp of the received message, and sent this information via RF link to a location server, which computed the smartphone position. Two environments were considered in the experiments: an office setup of 83 m^2, and a clear test area of 225 m^2. Six test points and 8 beacons were considered in the office setup, obtaining 95% errors below 16–29 cm, depending on the positioning algorithm used. 5 test points and 4 beacons were considered for the clear testing area, obtaining 95% errors below 40–66 cm. The AALTS system consisted of a similar architecture. In this case, the smartphone also calculated the Doppler shifts of the received signals [38], fusing all the information in a particle filter. Experiments were done in different environments with areas between 40 and 175 m^2. Different noise levels and beacon geometries were tested under static conditions. 95% of the errors ranged between 20–75 cm, depending on the noise and beacon geometry. Dynamic tests were also performed by following three different trajectories of up to 18 m length and covering ca. 36 m^2 of the total test area. They obtained deviations below 22–49 cm, for 90% of the measurements.

This article has been accepted for publication in a future issue of this journal, but has not been fully edited. Content may change prior to final publication. Citation information: DOI 10.1109/TIM.2021.3136261, IEEE Transactions on Instrumentation and Measurement

Besides academic prototypes, there are also some commercially available UIPS. The system from Hexamite consists of a set of transmitters and receivers, synchronized by an RF link [39]. The receivers, placed on the target, calculate the distances to the transmitters, which are sent via RF to a monitoring station. This station then calculates the position and orientation of the target. The IS-900 system from InterSense is used for tracking applications with a focus on industrial simulators and immersive displays, among others [40]. It fuses inertial navigation technologies with ultrasound signals to provide position and orientation of the target's attached tags. Marvelmind Robotics provides a UIPS where, in what they describe as non-inverse architecture (centralized), the target is equipped with a mobile beacon, which may also contain an IMU [41]. Four static beacons receive the ultrasonic signal from the mobile beacon, and location information is calculated by a central unit, which transmits it back to the target. The system can also work in inverse architecture mode (privacy-oriented), where the target is equipped with a receiver and calculates its own position from the ultrasonic signals transmitted by the beacons. Transmitters and receiver are synchronized by an RF link. This system was recently used in a structural health monitoring application using drones [42]. The centralized mode was used, and the ultrasonic ranges were fused with an IMU using a Kalman filter. For a squared trajectory in a room of approximately 170 m^2 and a true coverage area of 27.5 m^2, the reported errors at waypoints were below 20 cm.

III. The Forkbeard positioning system

The positioning system developed by Forkbeard Technologies AS consists of a network of beacons placed at strategic locations around the target area. This system positions standard iOS and Android smartphones using ultrasound and Bluetooth Low Energy (BLE) signals [43]. The positioning algorithm is build into an app (Forkbeard Lyra) which runs on the smartphone. The positioning also works while the app is running in the background or with the screen turned off. The beacons are battery powered with a claimed battery life of 10 years under the most adverse conditions [29].

The beacons are synchronized using RF communication. Each beacon transmits a locally unique, frequency-modulated ultrasonic signature at 1 second intervals. The signature has a duration of 10 ms and is modulated around a carrier frequency of 20.4 kHz. The transmit protocol is optimized to avoid audibility, by using low sound pressures and through suppression of sub-harmonics [44]. Due to this low carrier frequency, compared to standard RF protocols, the transmitted signals have a much longer duration and are therefore more prone to cross-interference. While the beacon signatures are selected to be locally unique, a combination of multiple reflections with Doppler shifts may degrade the phone's ability to identify signals unequivocally. The Forkbeard system minimizes such interference by assigning each beacon a different time offset for transmitting. In this system, a second is divided into 16 time slots of 60 ms each, plus 2.5 ms unused. This allows the system to maximize the physical distance between beacons transmitting at the same time, thereby minimizing the potential impact of signal interference. Both the frequency-modulated signature and time slot assignment are configured automatically using an optimization algorithm based on maximizing the distance between beacons with similar configurations. The update rate of the system can go up to 16.6 Hz (16 slots), depending on the number of allocated time slots and beacons in range. Since the transmission rate per beacon is fixed at one transmission per second, a small system with unallocated time slots will, on average, have a lower update rate.

The receiving device, a smartphone, communicates with the Forkbeard system using Wi-Fi or a cellular network [45]. The device is synchronized with the system and updated with relevant system information such as beacon IDs, positions and time slots. The positioning algorithm itself consists of three consecutive parts: raw audio processing, optimum range estimation per beacon, and finally position and velocity optimization of the device. Each part is described in further detail below.

A. Raw audio processing

The device listens continuously for raw audio signals in the ultrasonic spectrum. A signal is "detected" if its Received Signal Strength (RSS) exceeds a predefined threshold, whereupon its time-of-arrival (TOA) is stored in memory. The signal is correlated with a shaped window function to assess its validity. The shape of the window function corresponds to a generic ultrasonic signal which is expanded/compressed to coincide with the length of the received signal. Upon validation, the signal is decoded yielding the unique identifier of the transmitting beacon. Since detection range is limited due to attenuation effects, the time-of-transmission (TOT) is equal to the most recent time slot before TOA. Subtracting TOT from TOA yields the TOF of the signal. In addition, the Doppler shift is estimated by deconvolution of the received signal using the known code templates at various Doppler offsets. The deconvolution corresponding to the highest signal-to-noise (S/N) ratio is used to estimate the Doppler shift. The Doppler shift gives an indication of the radial "Doppler derived speed" (DDS), denoted v^r, which is the relative speed between the device and the beacon. Combining TOF, v^r and the local speed of sound c, the estimated range becomes

$$r = [c(T) - v^r] \cdot TOF \tag{1}$$

where T represents the temperature dependence of the speed of sound.

The intensity of an unobstructed sound wave is proportional to the inverse of its range squared, i.e. $I(r) \propto \frac{1}{r^2}$. Therefore, the computed range can be converted into an expected intensity value and compared to the RSS of the signal itself to estimate the probability of it being a line-of-sight (LOS) signal. A lower-than-expected intensity may indicate signal interference, obstructed LOS or reflected/non-LOS (NLOS), in which case the signal should be rejected. This comparison functions as an additional quality check, which, along with the deconvolution results, yields an overall probability weight w^p of the detected signal.

This article has been accepted for publication in a future issue of this journal, but has not been fully edited. Content may change prior to final publication. Citation information: DOI 10.1109/TIM.2021.3136261, IEEE Transactions on Instrumentation and Measurement

The final step is to group the processed data into a single *observation*, which consists of a timestamp (TOA), the estimated range r and DDS v^r, their respective standard deviations σ_r and σ_v, and the probability parameter w^p. The device maintains an independent observation buffer per beacon, and adds the new observation to its respective buffer. The set of observations is used to estimate the optimum range per beacon, described next.

B. Optimum range estimation

Optimum range estimation is an independent process per beacon based on its buffer of N historical observations. The idea is to extrapolate historical ranges towards a common point in time (timestamp of the most recent observation), thereby creating a set of quasi static ranges (QSR) whose weighted average yields the optimum range. In the following derivation, time t runs backwards starting from t_0, where t_0 corresponds to the most recent observation in the buffer. The i-indices indicate historical observations at t_i. The time between observations is approximately one second, though his may vary due to movement of the device and/or rejected observations. The objective is to find the optimum range and corresponding standard deviation at t_0, denoted $\overline{r}_0$ and $\overline{\sigma}_{r_0}$, based on the buffered data. This process consists of the following steps.

First, the change in range between t_i and t_0, described by the range increment dr_i, is calculated using numerical integration of the Doppler derived speeds. This is done by backwards integration,

$$dr_i = -\sum_{j=0}^{i-1} v_j^r \cdot (t_j - t_{j+1}), \tag{2}$$

Simpson's rule or a similar technique. The computed increments are added to their respective range estimates to obtain a set of QSR estimates $S_{QSR} = \left\{r_1^0, \cdots, r_N^0\right\}$, where

$$r_i^0 = r_i + dr_i, \tag{3}$$

is the QSR of r_i at t_0.

Next, the weight of each QSR, denoted w_i^q, is calculated based on the standard deviation (σ_{r_i}) and probability (w_i^p) of the underlying observation, a time-dependent weight w_i^t, and a fixed constant representing system uncertainty. The time-dependent weight is given by a linearly decreasing function based on the time difference between t_i and t_0. Starting from a value of one at $t_i = t_0$, it decreases towards zero at $(t_0 - t_i) = \Delta t_{max}$, the maximum length of the buffer. The system uncertainty σ_s is a general noise term which includes e.g. the physical limitations of the system and specific characteristics of the particular area. The weight of the QSR is given by

$$w_i^q = \frac{w_i^t \cdot w_i^p}{\sigma_{r_i}^2 + \sigma_s^2} \tag{4}$$

where the i-index indicates observation specific input data. The optimum beacon range and corresponding standard deviation can now be computed by taking the weighted mean and standard deviation over the elements of S_{QSR},

$$\overline{r}_0 = \sum_{i=1}^{N} \hat{w}_i^q r_i^0 \quad \text{and} \quad \overline{\sigma}_{r_0}^2 = \sum_{i=1}^{N} \hat{w}_i^q (r_i^0 - \overline{r}_0)^2 \tag{5}$$

where $\hat{w}_i^q$ are the normalized QSR weights.

In addition to $\overline{r}_0$ and $\overline{\sigma}_{r_0}$, an "overall" beacon weight W_0 is required as input to the cost function of the positioning algorithm. The beacon weight is based on the computed standard deviation $\overline{\sigma}_{r_0}$, the system uncertainty σ_s, and the sum of the time-dependent weights and probability parameters of the underlying observations,

$$W_0 = \frac{1}{\overline{\sigma}_{r_0}^2 + \sigma_s^2} \left[\sum_{i=1}^{N} w_i^t \cdot w_i^p\right]^2 \tag{6}$$

Note that W_0 depends on all data in the buffer, whereas the weights in (4) use single observations only.

The process described this far is based on a single, independent beacon with t_0 defined by its most recent observation. For a system composed of multiple beacons, there still remains a time difference between t_0 and the timestamp of the most recent observation system-wide, denoted t_0^*. The final step is thus to extrapolate the local optimum range towards this common timestamp shared by all beacons in the system. The extrapolation is a straightforward process based on the Doppler derived speed at t_0,

$$\overline{r}_0^* = \overline{r}_0 + v_0^r \Delta t \quad \text{and} \quad \overline{\sigma}_{r_0}^* = \sqrt{\overline{\sigma}_{r_0}^2 + \sigma_{v_0}^2 \Delta t^2} \tag{7}$$

where $\Delta t = t_0^* - t_0$. The most recent DDS and overall beacon weight remain unchanged during the extrapolation process ($v_0^{r*} = v_0^r$ and $W_0^* = W_0$). Applying the QSR estimation process to all beacons in the system yields a set of independent optimum beacon ranges, Doppler derived speeds, standard deviations and beacon weights at t_0^*. The next step is to convert these beacon ranges into a position and velocity estimate of the device.

C. Position and velocity estimation based on QSR

The aim of the positioning algorithm is to find the 3D position of the device at t_0^*. This is done by trilateration, where the weighted sum of squared residuals between the set of optimum ranges and the ranges derived from the proposed device position is minimized. From hereon, the device position and velocity, as well as beacon ranges, DDS and weights are given at t_0^*, and so the sub- and superscripts are dropped. Instead, i-indices now correspond to beacon number ($\overline{r}_{0,i}^* \rightarrow \overline{r}_i$). The cost function takes the form of a chi-square,

$$C(\boldsymbol{p}) = \sum_{i=1}^{N} W_i \left(R_i(\boldsymbol{p}) - \overline{r}_i\right)^2 \tag{8}$$

where $\boldsymbol{p}$ is the proposed device position, N the number of beacons, W_i the beacon weight, $\overline{r}_i$ the optimum range, and R_i the calculated range. The calculated range is given by

$$R_i(\boldsymbol{p}) = \|\boldsymbol{p} - \boldsymbol{b}_i\| \tag{9}$$

This article has been accepted for publication in a future issue of this journal, but has not been fully edited. Content may change prior to final publication. Citation information: DOI 10.1109/TIM.2021.3136261, IEEE Transactions on Instrumentation and Measurement

where $\|\cdot\|$ refers to the vector norm and $\boldsymbol{b}_i$ is the known position of the i-th beacon. Minimizing the cost function requires its derivative to be equal to zero,

$$\frac{\partial \mathbf{C}}{\partial \boldsymbol{p}} = \sum_{i=1}^{N} \frac{2W_i\left(R_i - \overline{r}_i\right)}{R_i}[\boldsymbol{b}_i - \boldsymbol{p}]^T = \mathbf{0}. \tag{10}$$

The global minimum of (8) is found by applying a quasi-Newton optimizer to solve (10). The starting point of the optimization process is typically provided by the last known position. The final result is the optimized device position $\overline{\boldsymbol{p}}$. In addition, the position error can be estimated from the residual of the optimization routine. Combined with the Hessian of (8), this produces a 3-by-3 position covariance matrix P_p. Error estimation allows for filtering of position measurements exceeding a certain predefined threshold.

The next step is to estimate the device velocity, denoted $\boldsymbol{v}$, from $\overline{\boldsymbol{p}}$ and the latest DDS per beacon v_i. This requires the directional unit vector between each individual beacon and the optimized device position,

$$\hat{\boldsymbol{m}}_i = \frac{1}{\overline{R}_i}(\boldsymbol{b}_i - \overline{\boldsymbol{p}}) \tag{11}$$

where $\hat{\boldsymbol{m}}_i$ is the directional unit vector of beacon i, and $\overline{R}_i$ follows from substituting $\boldsymbol{p} = \overline{\boldsymbol{p}}$ in (9). Vector $\hat{\boldsymbol{m}}_i$ runs parallel to the LOS between device and beacon, and represents the direction of the DDS in the frame of the phone. The directional unit vectors are combined into a weighted directional matrix $\hat{M} = [W_1\hat{\boldsymbol{m}}_1, \cdots, W_N\hat{\boldsymbol{m}}_N]^T$, where W_i are the beacon weights. In addition, the most recent DDS per beacon are combined into a single vector $\boldsymbol{v}^r = [v_1^r, \cdots, v_N^r]^T$. The optimized device velocity can now be described in terms of $\hat{M}$ and $\boldsymbol{v}^r$ as follows,

$$\overline{\boldsymbol{v}} = \hat{M}^{-1}\boldsymbol{v}^r \tag{12}$$

where $\hat{M}^{-1}$ is the pseudo-inverse of $\hat{M}$. The velocity covariance matrix can be computed in a similar way: defining P_{DDS} as the N-by-N diagonal matrix of DDS variances $\sigma_{v_i}^2$, we get

$$P_v = \hat{M}^{-1}P_{DDS}(\hat{M}^{-1})^T. \tag{13}$$

where P_v is the 3-by-3 covariance matrix of the device velocity.

The position $\overline{\boldsymbol{p}}$, velocity $\overline{\boldsymbol{v}}$ and their respective covariance matrices P_p and P_v are integrated into an Extended Kalman filter (EKF) framework. The propagation step is based on the current velocity, and the state corrections on new position and velocity measurements. The EKF setup allows the system to compute new position updates even when there are only two beacons in range, i.e. when the trilateration problem is technically under-determined.

D. Additional optimization techniques

The position optimization process can be extended by incorporating "landscape" information of the area. The landscape describes the physical boundaries (walls, floor and ceiling) and static obstacles (e.g., desks) which represent a reduced probability for the device position. The landscape is converted into a potential field based on costs associated to particular types of boundaries and obstacles [46]. Contrary to a binary obstacle cost, which changes instantaneously at the obstacle edge, a potential field is continuous and can be implemented directly into the optimization algorithm.

A further optimization constraint is the expected height of the device. Beacons are typically placed on a horizontal plane (ceiling), which generates large errors along the normal to that plane (vertical direction). Assigning a cost to deviations from the expected height reduces this effect. The default height is set to 1.2 m, which corresponds to a phone carried in the hand.

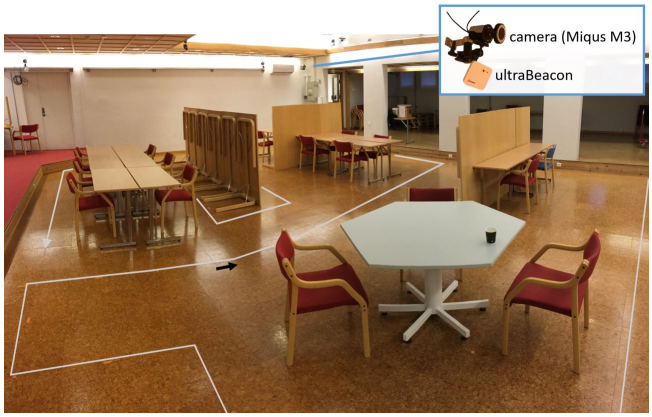

Fig. 1: An overview of the test area showing the "office" setup. Ground truth walking trajectory is given in light-grey.

TABLE I: Beacon coordinates and configurations

beacon	Coordinates			Beacon subsets					
no.	x (m)	y (m)	z (m)	10	8	6	5	4	3
1	-6.2	-11.1	2.1	✓	✓	✓	✓	✓	
2	0.1	-12.2	2.6	✓	✓	✓	✓		✓
3	6.4	-11.4	2.0	✓	✓	✓	✓	✓	
4	-3.1	-9.4	2.9	✓					
5	3.3	-9.4	2.9	✓					
6	-6.2	-3.0	2.1	✓	✓	✓	✓	✓	✓
7	-2.9	-4.0	2.4	✓	✓				
8	0.1	-5.8	2.4	✓	✓	✓			
9	3.0	-4.0	2.4	✓	✓				
10	6.0	-2.8	2.1	✓	✓	✓	✓	✓	✓
Beacon density (beacons / m^2):				0.07	0.06	0.04	0.03	0.03	0.02

IV. Experimental Setup

We tested the Forkbeard positioning system in a motion capture lab with a test area of approximately 150 m^2 (Fig. 1). The MoCap system uses 28 cameras providing up to 99 % coverage at sub-millimeter accuracy [47]. The Forkbeard installation consists of 10 beacons evenly distributed over the test area. An overview of the beacon positions is shown in Fig. 2. The beacons are attached to the ceiling or directly underneath the cameras, at a height of 2 to 3 m. The coordinates of the beacons are given in Table I.

Reduced systems, i.e., systems with less than 10 beacons, are described as modified configurations of the main system. We will use reduced systems to study the effect of beacon

This article has been accepted for publication in a future issue of this journal, but has not been fully edited. Content may change prior to final publication. Citation information: DOI 10.1109/TIM.2021.3136261, IEEE Transactions on Instrumentation and Measurement

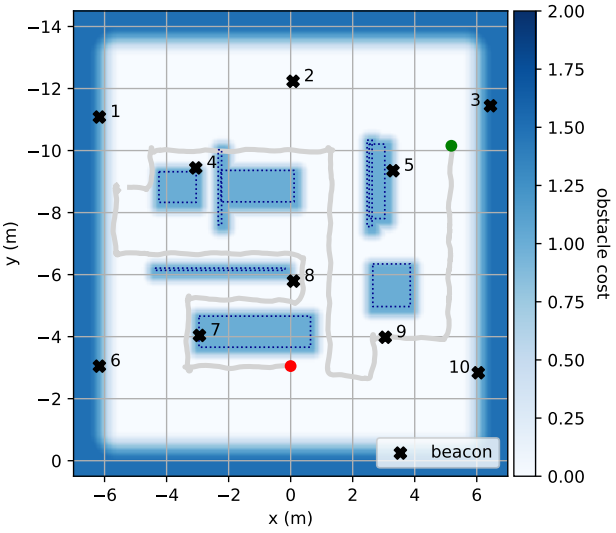

Fig. 2: Top view of the test area. Potential field of the obstacles and outer walls is given in blue. Ground truth trajectory is shown in grey, with the start and end points marked in green and red, respectively. Beacon positions are shown in black. Details on beacon coordinates and subsets are given in Table I.

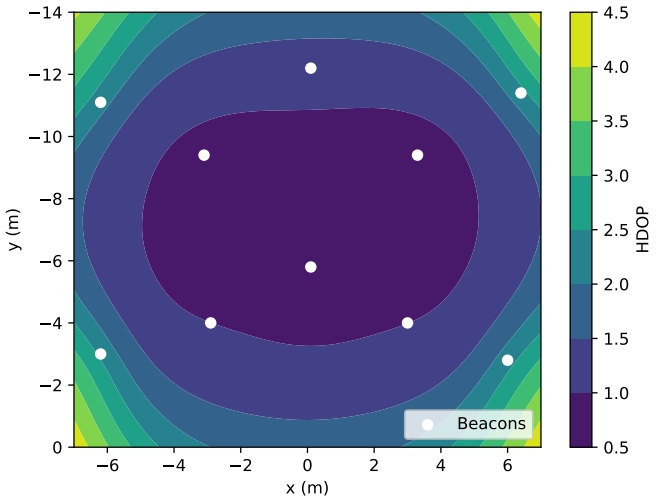

Fig. 3: Calculated HDOP for a 10-beacon setup. The results show a symmetric trend, with low dilution in the center and higher dilution towards the edges. This coincides with an evenly-distributed, mostly symmetric beacon geometry.

quantity and distribution on the accuracy of the positioning algorithm. The particular beacon subset per configuration is based on preliminary testing, which showed that using beacons on the perimeter generally produces better results. Configuration details are given in Table I. In practice, all beacons transmitted continuously throughout the experiments. That is, beacons were not physically turned off to create a reduced system. Instead, a modified recording of a reduced system was created by filtering out specific beacons during post-processing. This way, position estimates produced by a reduced system are still based on the same raw audio input. A potential concern here could be that the signals of the removed beacons are still present in the raw audio signal, causing interference. This effect, however, is negligible due to the locally unique signatures of the beacons, the differently allocated time slots, and the long time slot duration which minimizes reverberation effects.

Beacon geometry has a significant effect on the final positioning results. Preliminary insights into the differences between configurations can be obtained by computing the dilution-of-position (DOP) per configuration. Since we are interested in 2D positioning we limit ourselves to horizontal-dilution-of-position (HDOP) here. The results for the two main test cases, i.e. a 10- and 4-beacon configuration, are shown in Fig. 3 and Fig. 4, respectively. The main takeaways are that 1) the highest accuracy is expected in the center, and 2) the stability of the system goes down with decreasing number of beacons. Note, however, that the final positioning results are influenced by many more factors, such as attenuation, reflections, interference and noise.

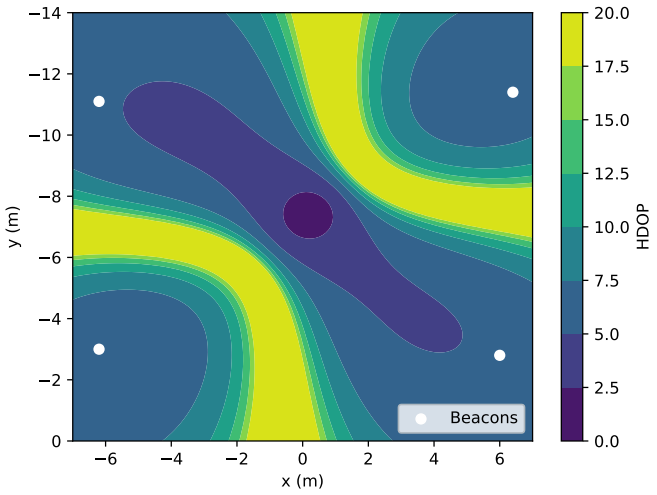

Fig. 4: Calculated HDOP for a 4-beacon setup. To improve visibility, HDOP values have been capped at a maximum value of 20. Compared to Fig. 3, the dilution is significantly higher. This can partly be explained by the lower beacon quantity. Interestingly, the results are not symmetric, even though the beacon positions approximately are. Additional evaluation, in which the beacon positions were altered slightly, produced a wide variety of HDOP trends. This implies that the 4-beacon setup is relatively unstable.

This article has been accepted for publication in a future issue of this journal, but has not been fully edited. Content may change prior to final publication. Citation information: DOI 10.1109/TIM.2021.3136261, IEEE Transactions on Instrumentation and Measurement

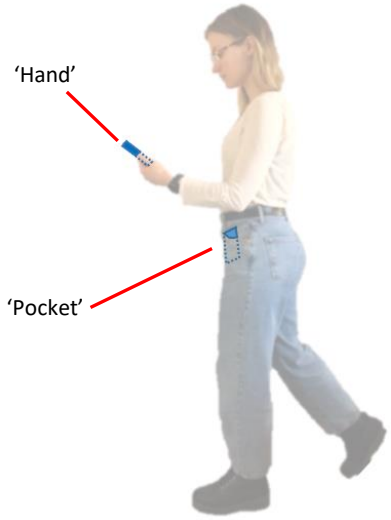

Fig. 5: Two phone positions used in this study: 1) phone in hand, and 2) phone in the left pocket.

The experiments are separated into two categories: static and dynamic. The static experiments are based on an equidistant grid of 73 points spread out over the floor of the test area. The ground truth reference of the grid points is based on the MoCap system. A smartphone was placed horizontally at each grid point on the floor for around 90 seconds, before moving it to the next grid point. This produced enough data to obtain 100 position measurements per grid point for any beacon configuration. For grid points with more than 100 position measurements, the first and last measurements were discarded to ensure stable conditions and avoid signal blockages. The dynamic experiments are based on a pedestrian carrying a smartphone, at an average walking speed of 0.8 m/s. Figure 2 shows the walking trajectory (42 m) used in all dynamic experiments. The trajectory was repeated five times per experiment, thereby generating five independent recordings. Each contains its own MoCap reference data to account for small deviations between recordings.

Two types of landscapes were considered. The first, referred to as the "clear" setup, consisted of an obstacle-free test area bounded by the walls, floor and ceiling. The second, referred to as the "office" setup, contained additional infrastructure in the form of chairs, desks and dividers (see Fig. 1). The cost of the outer walls was set to 1.5 and of additional obstacles to 1.0. Fig. 2 shows the potential field of the office setup. The static experiments were performed in the clear setup with the height constraint set to 0 m. For the dynamic experiments, we applied both setups and a height constraint of 1.2 m.

We used a Samsung Galaxy S9 for all experiments. For the dynamic experiments, we also recorded the specific force using the 3-axis accelerometer of the device. The specific force was then correlated with the acceleration obtained by the MoCap system to generate timestamps for the MoCap data based on the smartphone. This allowed us to compare the estimated positions generated by both systems under dynamic conditions, and calculate the position error. We further distinguish between two possible device positions for the dynamic experiments, as shown in Fig. 5. The first ("hand") is a device held in the hand. The second ("pocket") is a device in the left pocket.

V. Results

This section shows the results obtained from the characterization experiments. First, we will present the results under static conditions, where different beacon configurations have been taken into account. Next, we will present the results under dynamic conditions, evaluating different beacon configurations, two types of landscape, and the two phone positions over a repeated trajectory.

A. Characterization under static conditions

The results of the static experiments, in terms of accuracy and precision, are summarized in Fig. 6 for the 10-beacon configuration. This situation represents the best-case scenario for the system. Orange crosses mark the ground truth (grid points), whereas each individual position estimate provided by the Forkbeard system is represented by a blue circle. The figure includes two figures of merit: the 95% confidence ellipses are shown in red, and the errors between the averaged position and ground truth per grid point are depicted by black lines. The errors are calculated as the Euclidean distance between the grid point and the average of the estimated positions.

The upper-right area exhibits higher precision and accuracy than the left area. Based on the calculated HDOP values for a 10-beacon configuration (see Fig. 3), this behaviour cannot be explained by the beacon distribution. Furthermore, environmental conditions remained constant throughout the experiment: no air currents or significant temperature changes were observed. Therefore, we believe this behavior may be caused by small differences in orientation of the beacons, which, together with the limited aperture of the transducers, created coverage areas of different quality. Another explanation could be multipath components caused by nearby walls and columns. Two grid points in particular provide considerable worse positions than the rest, at (-2.15, -4.12) m, and (-4.54, -5.34) m. On those two grid points, the 95% ellipses overlap with their neighbours.

Next, we assessed the effect of the number of beacons on the system performance. The positions obtained with a 4-beacon configuration are shown in Fig. 7. Overall, the precision and accuracy of the 4-beacon configuration are slightly worse compared to the 10-beacon configuration, as may be expected from the higher HDOP values (see Fig. 4). This is reflected by the 95% ellipses, which exhibit a larger area in most cases.

For a smoother visualization, and to gain a better insight into the error distribution, we interpolated the average error per grid point over a denser grid of 100×100 grid points. The resulting heat maps are shown in Figures 8 and 9 for the 10-beacon and the 4-beacon configuration, respectively. For the 10-beacon configuration, the largest errors are between 63-93 cm and primarily related to the aforementioned two problematic grid points. The upper-right area exhibits lower average errors, generally below 30 cm with a minimum value of 13 cm. The maximum error of the 4-beacon configuration is 1.58 m at

This article has been accepted for publication in a future issue of this journal, but has not been fully edited. Content may change prior to final publication. Citation information: DOI 10.1109/TIM.2021.3136261, IEEE Transactions on Instrumentation and Measurement

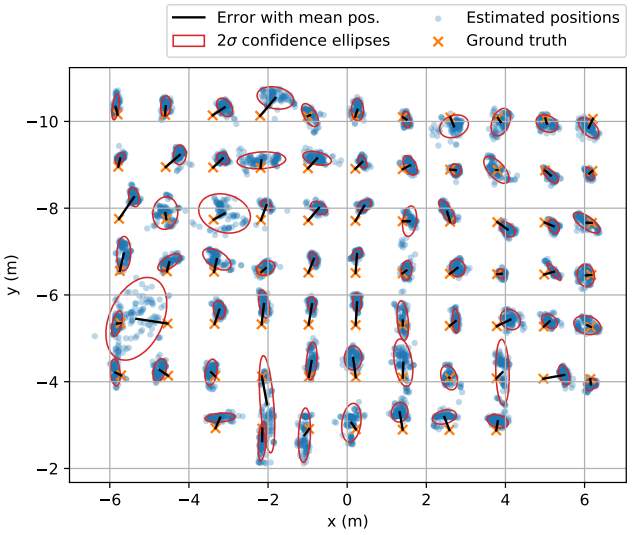

Fig. 6: Static positions obtained with the 10-beacon configuration. Each grid point (orange cross) contains 100 position estimates by the Forkbeard system (blue circles). Mean error distance is given in black, and 95% confidence ellipses in red.

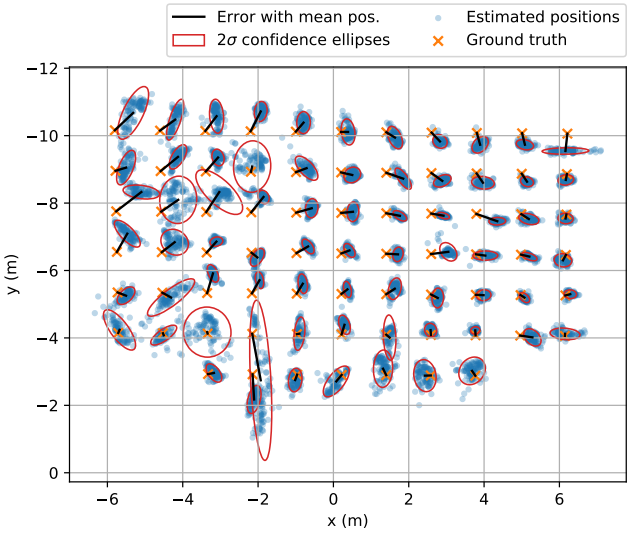

Fig. 7: Static positions obtained with the 4-beacon configuration. Each grid point (orange cross) contains 100 position estimates by the Forkbeard system (blue circles). Mean error distance is given in black, and 95% confidence ellipses in red.

the problematic grid point at (-2.15, -4.12) m, whereas the minimum error is 14 cm on the right area. Interestingly, the second problematic point exhibits a better behavior now than with the 10-beacon configuration. This seems counter-intuitive since the HDOP values worsen when going from a 10- to a 4-beacon configuration. However, we believe that this behavior may be caused by poor range estimations introduced by one or more of the removed six beacons. For instance, due to a particular multipath interference from nearby walls towards this point.

Finally, we calculated the Euclidean distance between all

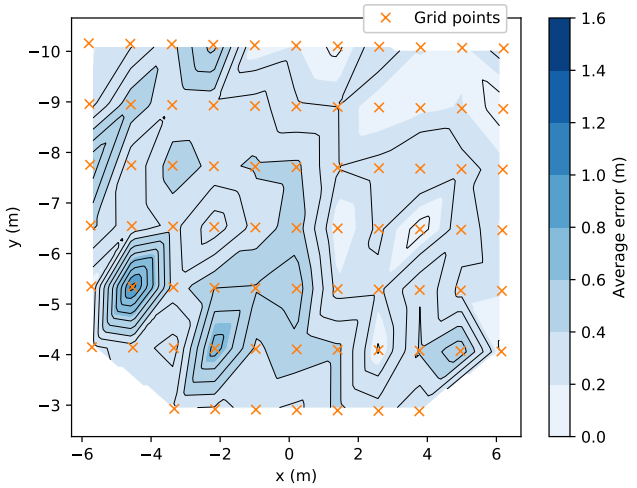

Fig. 8: Average error heat map for the 10-beacon configuration.

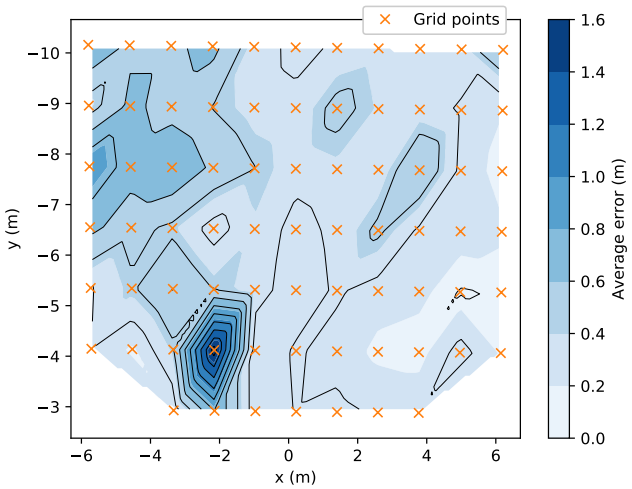

Fig. 9: Average error heat map for the 4-beacon configuration.

estimated positions with regard to their corresponding ground truth to obtain the absolute errors. This was done for all configuration described in Table I. The results are gathered in Fig. 10, which shows the Cumulative Distribution Function (CDF) of the position errors per configuration. It can be seen that 95% of the obtained positions, marked by the black-dashed line, have errors below 65 cm when using 10 beacons. This error increases to 1.12 m when reducing the number of beacons to 3. Nevertheless, it seems that there is not so much difference in the system performance when using 4–8 beacons, although all of these produce slightly larger errors than the 10-beacon configurations. A small increase in the performance at the 95% level when using 5 beacons instead of 8, can again be caused by the removal of beacons that introduce erroneous estimations in the TOF calculation. Table II summarizes the results of all beacon configurations at the 95, 80 and 68% levels. While the CDFs show similar trends for configurations above 4 beacons, it is important to note that reduced systems provide a lower update rate. Furthermore, these systems will be more sensitive to losing individual beacons due to an

This article has been accepted for publication in a future issue of this journal, but has not been fully edited. Content may change prior to final publication. Citation information: DOI 10.1109/TIM.2021.3136261, IEEE Transactions on Instrumentation and Measurement

obstructed line-of-sight. While the first issue may be resolved by designing the time slots to be contiguous, this will not resolve the second issue.

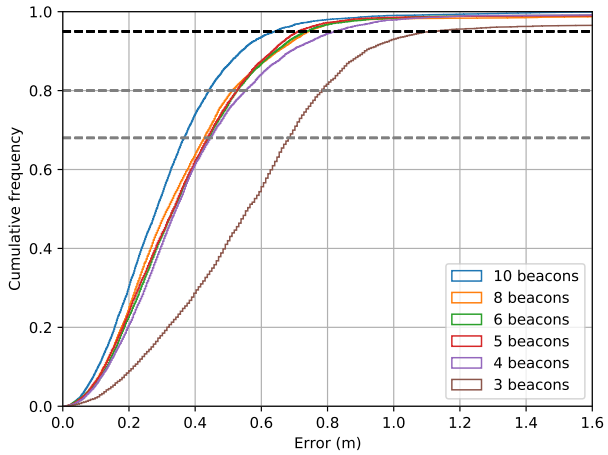

Fig. 10: CDF of the absolute errors produced by the static experiments, per beacon configuration. The black-dashed line indicates the 95% level, whereas the 80 and 68% levels are indicated by grey-dashed lines.

TABLE II: Maximum error at different levels - static

No. of beacons	Error (m) 95%	80%	68%
10	0.64	0.44	0.37
8	0.74	0.51	0.43
6	0.73	0.53	0.44
5	0.71	0.53	0.44
4	0.82	0.55	0.45
3	1.12	0.78	0.68

B. Characterization under dynamic conditions

The second part involves experiments performed under dynamic conditions. Each experiment consists of five separate recordings along the trajectory shown in Fig. 2. The dynamic experiments are defined by phone position (“hand” or “pocket”), landscape (“clear” or “office”) and number of beacons (3 to 10). A phone in hand provides better microphone exposure than a phone in the pocket. Furthermore, a clear landscape contains less reflective surfaces than an office setup. Therefore, we will focus on the following two cases: case I is a clear setup with phone in hand (best case), whereas case II is an office setup with phone in the pocket (worst case).

Figure 11 shows the five trajectories obtained for case I and a 10-beacon configuration. Measurements with estimated errors above 1.5 m, as internally computed by the positioning algorithm described in Section III, have been filtered out. The removed data constitute 56 measurements (ca. 2%) out of a total of 2650 measurements. All trajectories follow the ground truth reference well with some notable exceptions: track 3 contains a series of large offset points in the middle of the test area, all tracks seem to drift slightly outwards at the top, and the bottom-left is the main problem area for all tracks. The last observation coincides with what was observed in the static experiments.

Both cases were tested against all beacon configurations. The resulting CDFs are shown in Fig. 12 for case I and Fig. 13 for case II. It is apparent in both figures that accuracy is not linearly correlated with beacon quantity, once a minimum of four (case I) or five (case II) beacons has been reached. Note, however, that the update rate does increase with beacon quantity, allowing for stricter filtering criteria. The 3-beacon configuration stands out negatively in both cases, as might be expected: An erroneous range measurement, caused by e.g., an obstructed line-of-sight and a strong multipath, weighs heavier when there are fewer other range measurements to compensate. This effect is also apparent for the 4-beacon configuration in case II, though not as strongly. The results are summarized in Table III, which gives the maximum error considering 95, 80, and 68%.

While the general trend reflects the initial observations, a noticeable exception is the 95% level of the 10-beacon configuration in case II. To gain a better insight into the specific problem areas, we divided the test area into bins of 25×25 cm. The average absolute distance error per bin was then computed based on the ground truth of the five trajectories per experiment. The results for case I with a 10-beacon configuration are shown in Fig. 14a. The results for a reduced configuration of 4 beacons are shown in Fig. 14b. The differences between the figures are small. While the 10-beacon configuration contains more problematic areas, the overall error is slightly lower than for the 4-beacon configuration. The results for case II are shown in Fig. 14c (10 beacons) and Fig. 14d (4 beacons). The advantage of increased number of beacons is more apparent here. Overall, the 10-beacon configuration contains lower errors, with the exception of the right side of the map. This could be the result of the phone being carried in the left pocket. While the pedestrian blocks the direct line-of-sight for beacons on the left, their signals may still reach the phone via a multipath, using the wall on the right. Since more beacons are affected by this in the 10-beacon configuration than in the 4-beacon configuration, larger errors may be produced in the former configuration.

The effects of multipath, noise and attenuation can be investigated further by considering the individual set of valid beacon ranges per position estimate. That is, a position estimate is not always based on all available beacons. If the probability of a range measurement being a true LOS measurement is low, e.g. due to an unexpected RSS value, then the beacon is excluded from the trilateration process of that particular position estimate. For example, position estimates in the first 10 seconds of the trajectory (straight path on the right side of the test area) are typically based on 9-10 (all) beacon ranges for case I, but only on 7-9 ranges for case II, considering a 10-beacon configuration. This means that up to three beacons did not provide a valid LOS range measurement according to the algorithm. In the most problematic area, around (-3, -5) m, the set of valid ranges goes down to 3-6 beacons for case II. In other words, between four to seven beacons produced NLOS ranges and were thus rejected. For the 4-beacon configuration,

This article has been accepted for publication in a future issue of this journal, but has not been fully edited. Content may change prior to final publication. Citation information: DOI 10.1109/TIM.2021.3136261, IEEE Transactions on Instrumentation and Measurement

position estimates for case I are generally based on 3-4 beacons, whereas case II positions are often limited to 2-3 beacon ranges. The latter explains the large errors along the entire trajectory in Fig. 14d. Note that the above observations depend on proper filtering of LOS/NLOS signals. This may not always be the case, resulting in occasional erroneous position estimates.

Besides accuracy, another important aspect of a positioning system is its consistency, here defined as the ability to generate a constant stream of position updates at a predefined update rate. We tested the consistency of the system by setting the target update rate to 1 Hz. For each 1-second time interval, we take the measurement with the smallest error (as estimated by the internal Forkbeard algorithm) and discard the rest. If the interval contains no measurements, then the default error is set to > 1.5 m. The results for the 10- and 4-beacon configurations (Case II - filtered) are shown in Fig. 14e and 14f. Since the 10-beacon configuration has a potential update rate of 10 measurements per second, and the 4-beacon configuration has a maximum rate of 4, we expect more "gaps" in the latter configuration, which will appear as red blocks. From the two figures we see that this is indeed the case. The 10-beacon configuration gives a near-continuous trajectory, whereas the 4-beacon configuration shows many gaps. Comparing the filtered results with the non-filtered results (Fig. 14c and 14d), we see that the consistent update rate has a minor effect on the 10-beacon configuration, whereas the results for the 4-beacon configuration are significantly worse.

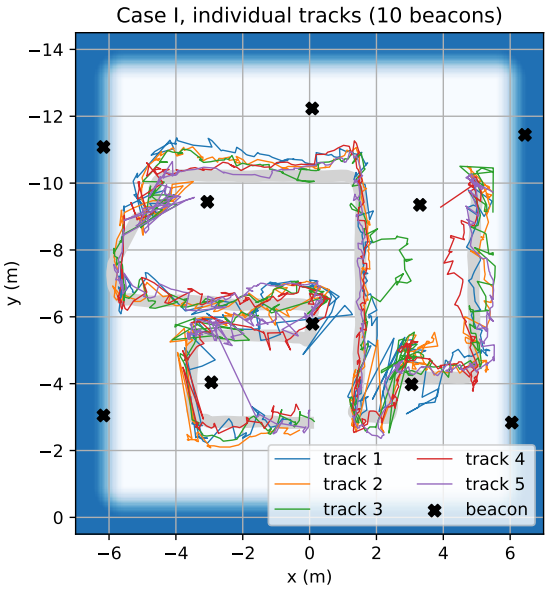

Fig. 11: A set of five independent trajectories computed by the Forkbeard system. The trajectories shown here are based on a clear area, with the phone carried in the hand (case I) and a 10-beacon configuration. The average walking speed was 0.8 m/s. Errors over 1.5 m have been filtered out.

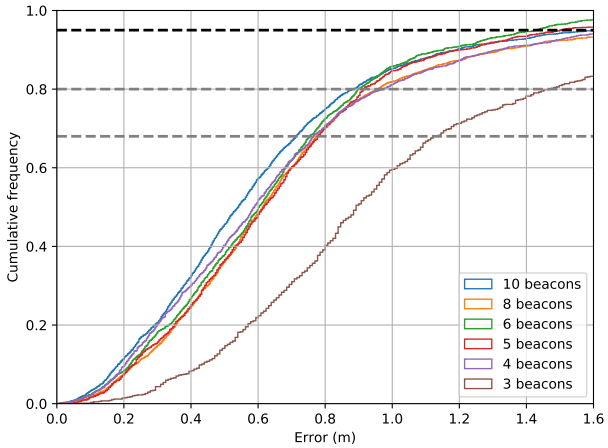

Fig. 12: CDF for case I (clear area with phone in hand) of the dynamic experiments for different beacon configurations. The black-dashed line indicates the 95% level, with the 80% and 68% levels given by grey-dashed lines.

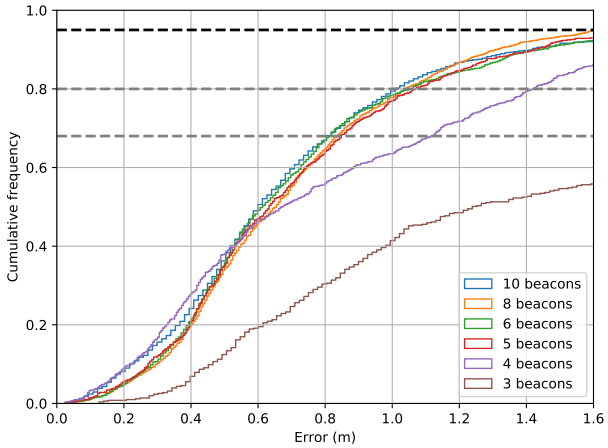

Fig. 13: CDF for case II (office setup with phone in pocket) of the dynamic experiments for different beacon configurations. The black-dashed line indicates the 95% level, with the 80% and 68% levels given by grey-dashed lines.

TABLE III: Maximum errors at different levels - dynamic

No. of beacons	Error (m) case I 95%	case I 80%	case I 68%	case II 95%	case II 80%	case II 68%	case II 68%[1]
10	1.63	0.88	0.71	2.54	1.02	0.82	1.01
8	1.91	0.96	0.78	1.64	1.04	0.84	1.07
6	1.43	0.9	0.76	1.94	1.06	0.82	1.09
5	1.51	0.92	0.78	1.91	1.07	0.85	1.38
4	1.69	0.98	0.77	2.24	1.43	1.12	1.55
3	5.23	1.48	1.14	6.61	4.36	2.73	2.21

[1] Positions based on ultrasound only (potential field disabled).

VI. Conclusions

This work describes an extensive evaluation of the commercial indoor positioning system developed by Forkbeard Technologies AS. The system performance has been assessed

This article has been accepted for publication in a future issue of this journal, but has not been fully edited. Content may change prior to final publication. Citation information: DOI 10.1109/TIM.2021.3136261, IEEE Transactions on Instrumentation and Measurement

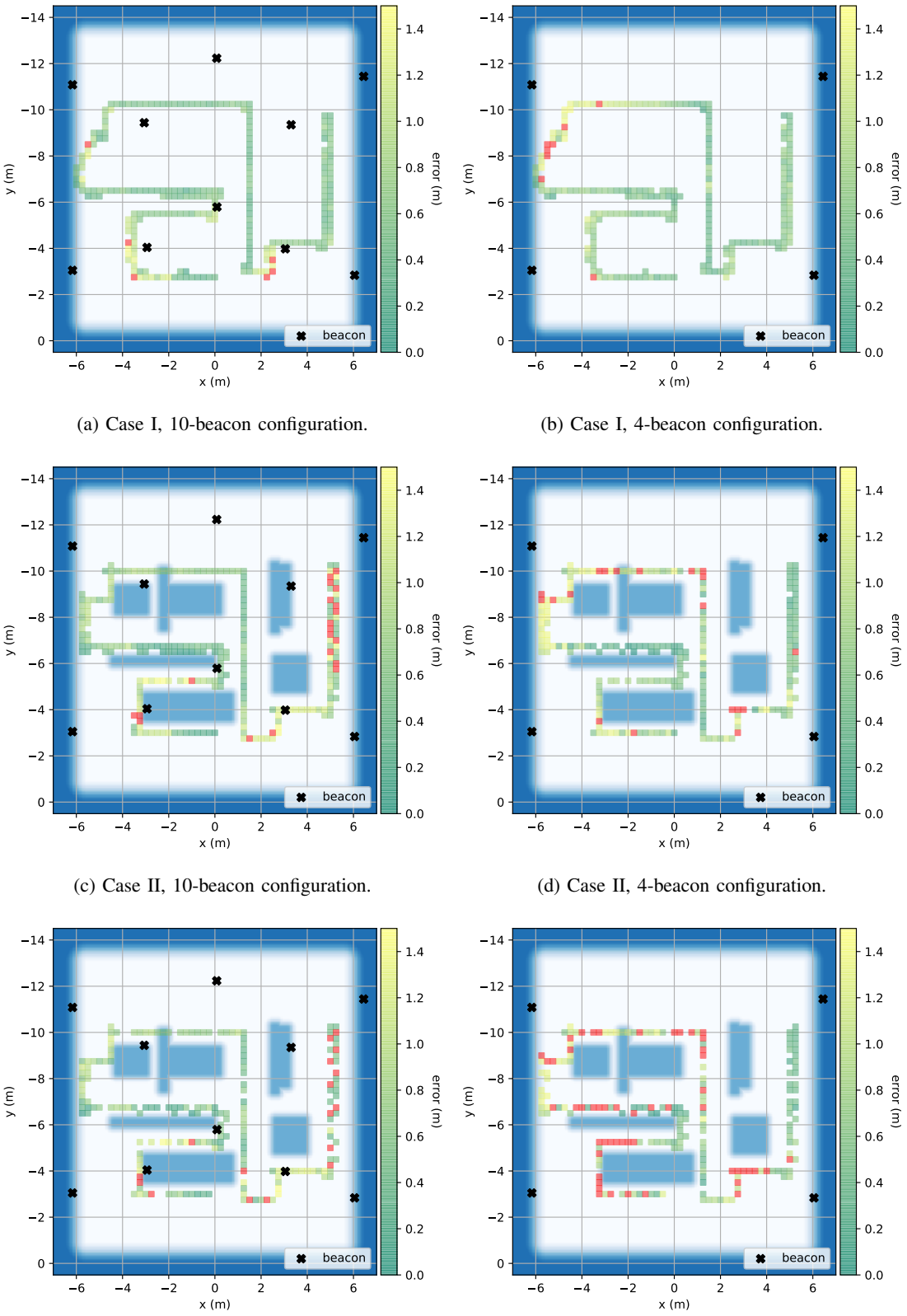

(a) Case I, 10-beacon configuration.

(b) Case I, 4-beacon configuration.

(c) Case II, 10-beacon configuration.

(d) Case II, 4-beacon configuration.

(e) Case II, 10-beacon configuration, filtered to 1 Hz.

(f) Case II, 4-beacon configuration, filtered to 1 Hz.

Fig. 14: 2D error maps of the dynamic experiments (average walking speed: 0.8 m/s). Top row: phone in hand (Case I). Middle row: phone in pocket with obstacles (Case II). Bottom row: Case II with constant update rate at 1 Hz. 10-beacon configuration on the left, 4-beacon configuration on the right. Each figure contains the data of five independent trajectories, divided over bins of 25×25 cm. Each colored bin contains at least one measurement. Errors larger than 1.5 m are shown in red. Comparison between (d) and (f) shows that a 4-beacon configuration is insufficient to produce a stable update rate at 1 Hz.

under static and dynamic conditions, for different beacon configurations, test landscapes and phone positions on the carrier. We performed a statistical analysis under static conditions using a grid of 73 points and 100 measurements per grid point. Positioning errors were found to be below 44 cm when using 10 beacons, and below 55 cm when using 4 beacons, considering 80% of the measurements. Considering 95% of the measurements, the errors increased to 64 cm and 82 cm, respectively.

For evaluation under dynamic conditions, we used a walking trajectory of 42 m, covering an area of 80 m^2. Each experiment was repeated five times. The observed positioning errors were up to 88 cm (10 beacons) and 98 cm (4 beacons) for a hand-carried phone in an obstacle-free test area, considering 80% of the measurements. The most challenging condition, i.e, a phone in the pocket and an "office" setup, produced errors up to 102 cm and 143 cm, respectively. Applying a filter to obtain a consistent update rate shows that adding beacons to the system improves the reliability significantly.

These results are comparable to those obtained by academic prototypes that considered similar acoustic frequencies, test areas and smart devices [35]–[38]. Two main factors may account for the differences in accuracy: 1) The number of grid points considered for evaluation under static conditions. The system in [36] considered 25 points, five and six test points were used in [35], and eight in [38]. 2) The trajectory length and true coverage area of the dynamic experiments. The trajectory in [37] was 14 m, and the longest trajectory in [38] ca. 20 m. Both covered an area of approximately 35 m^2.

The positioning algorithm evaluated here is based on ultrasonic ranges and floor plan information. While it uses BLE for communication between beacons and the smartphone, it is not part of the positioning engine itself. Furthermore, the system does not utilize other sensors available in the smartphone, most notably the IMU. Future work could focus on improving the algorithm by fusing the ultrasonic ranges with BLE, IMU, and other sensor data. In addition to increasing positioning accuracy, this could improve reliability and lower the cost by reducing the number of beacons required.

Acknowledgements

The authors would like to thank Forkbeard Technologies AS for providing the hardware for the experiments, as well as information and support regarding the system operation.

References

[1] M. N. K. Boulos and G. Berry, "Real-time locating systems (RTLS) in healthcare: a condensed primer," *Int. J. Health Geogr.*, vol. 11, no. Article number 25, pp. 1–8, 2012.

[2] N. Ferracuti, C. Norscini, E. Frontoni, P. Gabellini, M. Paolanti, and V. Placidi, "A business application of RTLS technology in Intelligent Retail Environment: Defining the shopper's preferred path and its segmentation," *J. Retailing and Consumer Services*, vol. 47, pp. 184–194, 2019.

[3] S. Kohlbrecher, O. von Stryk, J. Meyer, and U. Klingauf, "A flexible and scalable SLAM system with full 3D motion estimation," in *Proc. IEEE Int. Symp. SSRR*, Kyoto, Japan, Nov. 2011, pp. 155–160.

[4] Technavio, "Global RTLS market in the transportation and logistics sector 2016-2020," last accessed on: December 8, 2021. [Online]. Available: https://www.technavio.com/report/global-machine-machine-m2m-and-connected-devices-global-rtls-market-transportation-and

[5] T.R. Hellmich MD *et al.*, "Contact tracing with a real-time location system: A case study of increasing relative effectiveness in an emergency department," *Am. J. Infect. Control*, vol. 45, pp. 1308–1311, 2017.

[6] C.T. Nguyen *et al.*, "A comprehensive survey of enabling and emerging technologies for social distancing - Part I: Fundamentals and enabling technologies," *IEEE Access*, vol. 8, pp. 153 479–153 507, 2020.

[7] ——, "A comprehensive survey of enabling and emerging technologies for social distancing - Part II: Emerging technologies and open issues," *IEEE Access*, vol. 8, pp. 154 209–154 236, 2020.

[8] Markets and Markets, "Indoor location market worth $17.0 billion by 2025," last accessed on: December 8, 2021. [Online]. Available: https://www.marketsandmarkets.com/PressReleases/indoor-location.asp

[9] J. Blankenbach and A. Norrdine, "Position estimation using artificial generated magnetic fields," in *Proc. Int. Conf. IPIN*, Zürich, Switzerland, Sept. 2010, pp. 1–5.

[10] S.-C. Yeh, W.-H. Hsu, W.-Y. Lin, and Y.-F. Wu, "Study on an indoor positioning system using Earth's magnetic field," *IEEE T. Instrum. Meas.*, vol. 69, no. 3, pp. 865–872, 2020.

[11] G. Martín Mendoza-Silva, J. Torres-Sospedra, and J. Huerta, "A meta-review of indoor positioning systems," *Sensors-Basel*, vol. 19, no. ID 4507, pp. 1–45, 2019.

[12] Y. Wu, H.-B. Zhu, Q.-X. Du, and S.-M. Tang, "A survey of the research status of pedestrian dead reckoning systems based on inertial sensors," *Int. J. Autom. Comput.*, vol. 16, no. 1, pp. 65–83, 2018.

[13] J.-S. Lee and S.-M. Huang, "An experimental heuristic approach to multi-pose pedestrian dead reckoning without using magnetometers for indoor localization," *IEEE Sens. J.*, vol. 19, no. 20, pp. 9532–9542, 2019.

[14] N. Ravi, P. Shankar, A. Frankel, A. Elgammal, and L. Iftode, "Indoor localization using camera phones," in *Proc. IEEE WMCSA*, Orcas Island, WA, USA, Aug. 2005, pp. 1–7.

[15] M. Sun, L. Zhang, Y. Liu, X. Miao, and X. Ding, "See-Your-Room: Indoor localization with camera vision," in *Proc. ACM TURC*, Chengdu, China, May 2019, pp. 1–5.

[16] A. D. Cheok and L. Yue, "A novel light-sensor-based information transmission system for indoor positioning and navigation," *IEEE T. Instrum. Meas.*, vol. 60, no. 1, pp. 290–299, 2011.

[17] F. Alam, M. T. Chew, T. Wenge, and G. S. Gupta, "An accurate visible light positioning system using regenerated fingerprint database based on calibrated propagation model," *IEEE T. Instrum. Meas.*, vol. 68, no. 8, pp. 2714–2723, 2019.

[18] G. Chen, X. Meng, Y. Wang, Y. Zhang, P. Tian, and H. Yang, "Integrated WiFi/PDR/Smartphone using an unscented Kalman filter algorithm for 3D indoor localization," *Sensors-Basel*, vol. 15, no. 9, pp. 24 595–24 614, 2015.

[19] M. B. Del Rosario, N. H. Lovell, and S. J. Redmond, "Quaternion-based complementary filter for attitude determination of a smartphone," *IEEE Sens. J.*, vol. 16, no. 15, pp. 6008–6017, 2016.

[20] G. Gomes and H. Sarmento, "Indoor location system using ZigBee technology," in *Proc. Int. Conf. SENSORCOMM*, Athens, Greece, Jun. 2009, pp. 152–157.

[21] M. Uradzinski, H. Guo, X. Liu, and M. Yu, "Advanced indoor positioning using Zigbee wireless technology," *Wireless Pers. Commun.*, vol. 97, no. 4, pp. 6509–6518, 2017.

[22] R. Faragher and R. Harle, "Location fingerprinting with Bluetooth Low Energy beacons," *IEEE J. Sel. Area. Comm.*, vol. 33, no. 11, pp. 2418–2428, 2015.

[23] C. Zhou, J. Yuan, H. Liu, and J. Qiu, "Bluetooth indoor positioning based on RSSI and Kalman filter," *Wireless Pers. Commun.*, vol. 96, no. 3, pp. 4115–4130, 2017.

[24] A. Khalajmehrabadi, N. Gatsis, and D. Akopian, "Modern WLAN fingerprinting indoor positioning methods and deployment challenges," *IEEE Commun. Surv. Tut.*, vol. 19, no. 3, pp. 1974–2002, 2017.

[25] A. Jiménez and F. Seco, "Comparing Ubisense, BeSpoon, and DecaWave UWB Location Systems: Indoor Performance Analysis," *IEEE T. Instrum. Meas.*, vol. 66, no. 8, pp. 2106–2117, 2017.

[26] Y. Bai, L. Lu, J. Cheng, J. Liu, Y. Chen, and J. Yu, "Acoustic-based sensing and applications: A survey," *Comput. Netw.*, vol. 181, no. ID 107447, pp. 1–19, 2020.

[27] R. Carotenuto, M. Merenda, D. Iero, and F. Della Corte, "An indoor ultrasonic system for autonomous 3-D positioning," *IEEE T. Instrum. Meas.*, vol. 68, no. 7, pp. 2507–2518, 2019.

[28] J. Aparicio, T. Aguilera, and F. Álvarez, "Robust airborne ultrasonic positioning of moving targets in weak signal coverage areas," *IEEE Sens. J.*, vol. 20, no. 21, pp. 13 119–13 130, 2020.

[29] Forkbeard Technologies AS, last accessed on: December 8, 2021. [Online]. Available: https://forkbeardtech.com/technology/

[30] W. Moritz, P. Shreve, and L. Mace, "Analysis of an ultrasonic spatial locating system," *IEEE T. Instrum. Meas.*, vol. 25, no. 1, pp. 43–50, 1976.

[31] B. Everett, "A multi-element ultrasonic ranging array," 1985, department of the Navy, Naval Sea Systems Command, Tech. Rep. NAVSEA No. 450-90G-TR-0001.

[32] F. Figueroa and J. Lamancusa, "A method for accurate detection of time of arrival: Analysis and design of an ultrasonic ranging system," *J. Acoust. Soc. Am*, vol. 91, no. 1, pp. 486–494, 1992.

[33] M. Drumheller, "Mobile robot localization using sonar," *IEEE T. Pattern Anal.*, vol. PAMI-9, no. 2, pp. 325–332, 1987.

[34] L. Kleeman, "Ultrasonic autonomous robot localization system," in *Proc. IEEE/RSJ Int. Workshop IROS*, Tsukuba, Japan, 1989, pp. 212–219.

[35] Y. Wang, J. Li, R. Zheng, and D. Zhao, "ARABIS: An asynchronous acoustic indoor positioning system for mobile devices," in *Proc. Int. Conf. IPIN*, Sapporo, Japan, 2017, pp. 1–8.

[36] P. Lazik and A. Rowe, "Indoor pseudo-ranging of mobile devices using ultrasonic chirps," in *Proc. 10th ACM Conf. SenSys*, Toronto, Canada, 2012, pp. 99–112.

[37] A. Ens, F. Höflinger, J. Wendeberg, J. Hoppe, R. Zhang, A. Bannoura, L. M. Reindl, and C. Schindelhauer, "Acoustic self-calibrating system for indoor smart phone tracking," *Int. J. Navigation and Observation*, vol. 2015, no. Article ID 694695, pp. 1–15, 2015.

[38] C. Cai, R. Zheng, J. Li, L. Zhu, H. Pu, and M. Hu, "Asynchronous acoustic localization and tracking for mobile targets," *IEEE Internet Things*, vol. 7, no. 2, pp. 830–845, 2020.

[39] Hexamite, "Hx19 RFID Ultrasonic Positioning," last accessed on: December 8, 2021. [Online]. Available: https://www.hexamite.com/hx19posa.htm

[40] InterSense, "IS-900," last accessed on: December 8, 2021. [Online]. Available: https://www.intersense.com/wp-content/uploads/2020/09/Thales_InterSense_IS-900_V2_Data_Sheet_2020-09.pdf

[41] Marvelmind Robotics, last accessed on: December 8, 2021. [Online]. Available: https://marvelmind.com/pics/marvelmind_presentation.pdf

[42] D. Kang and Y.-J. Cha, "Autonomous UAVs for structural health monitoring using deep learning and an ultrasonic beacon system with geo-tagging," *Comput-aided Civ. Inf.*, vol. 33, no. 10, pp. 885–902, 2018.

[43] W. E. Booij and C. Antille, "An optimal positioning engine for an acoustic ranging system," US Patent, apl. nr. PCT/GB2020/052049.

[44] W. E. Booij, "Orthogonal frequency scheme for narrowband acoustic signalling," US Patent, apl. nr. US 16/580268.

[45] W. E. Booij, K. Haslum, F. B. Engelhardtsen, and E. Bakke, "Low level smartphone audio and sensor clock synchronization," US Patent WO2019/145 922, apl. nr. PCT/IB2019/050679.

[46] W. E. Booij, C. Antille, and H. M. Ewald, "Static potentials in the positioning cost function-landscaping," US Patent, apl. nr. PCT/GB2021/050046.

[47] Qualisys, last accessed on: December 8, 2021. [Online]. Available: https://www.qualisys.com/

Vincent Thio received a MSc degree in geophysics from Utrecht University, the Netherlands, in 2015. From 2016 to 2018, he worked as a Reservoir Engineer for Shell. He is currently pursuing a PhD degree in physics at the University of Oslo, Norway. His research interests include indoor localization and navigation, ultrasound-based positioning and sensor fusion.

Joaquín Aparicio (M'17) received his Physics degree from the University of Extremadura, Badajoz, Spain, in 2008, and his PhD degree in Electronics from the University of Alcalá, Alcalá de Henares, Spain, in 2014. From 2015 to 2018 he was a Postdoctoral Researcher at the Japan Agency for Marine-Earth Science and Technology, Yokosuka, Japan. Since 2018 he is a Postdoctoral Fellow at the Department of Informatics, University of Oslo, Oslo, Norway. His research interests are acoustic positioning and communication systems, acoustic propagation and signal processing, for both indoor and underwater environments.

Kjetil Bergh Ånonsen is a senior scientist in the navigation group at the Norwegian Defense Research Establishment (FFI). He holds a PhD in Engineering cybernetics and an MSc in applied mathematics from the Norwegian University of Science and Technology (NTNU). He joined FFI in 2007.

Jan Kenneth Bekkeng received the Ph.D. degree in Physics from the University of Oslo, Norway, in 2007, working within the fields of spacecraft attitude determination and instrumentation. He joined the Norwegian Defence Research Establishment (FFI) in 2007 and became a Principal Scientist in 2016. He also joined the Department of Physics, University of Oslo, as a researcher in 2007. He became an Associate professor II in 2010. His current research interests include electronic warfare, infrared and electro-optical systems, missiles, modelling and simulation, estimation, navigation and tracking. He is a member of technical teams in NATO, including NATO Science and Technology Organization (STO).